

Hybrid MAPbI₃ Perovskite Growth Mechanism from Irregular Particles to Cuboid and Hopper-Type Morphologies

Ariany Bonadio^{1b}^a and Jose A. Souza^{1b}^{*,a}

^aCentro de Ciências Naturais e Humanas, Universidade Federal do ABC (UFABC),
09210-580 Santo André-SP, Brazil

Methylammonium lead iodide (MAPbI₃), used as light-harvesting layer in solar cell devices, has attracted great attention from scientific community due to its excellent photovoltaic performance. In this work, we have shown a comprehensive study on the hybrid organic-inorganic MAPbI₃ perovskite growth mechanism from irregular small particles to cuboid shape followed by hopper-type morphology through a systematically change on both the temperature and lead source concentration during the solution synthesis process. Indeed, we have observed very interesting hopper growth resulting in a pyramid-hollow like morphology. We have explained the morphology evolution by taking into account thermodynamics growth, which compete with kinetics growth under nonequilibrium conditions.

Keywords: perovskite, crystal growth, morphology evolution, hopper morphology

Introduction

The hybrid organic-inorganic perovskites have attracted great attention from scientific community due to their unique electronic and optical properties which brought about excellent photovoltaic performance.^{1,2} Methylammonium lead iodide (MAPbI₃, where MA = CH₃NH₃⁺) has been the most studied material in this family and has been widely used as an absorber layer of perovskite solar cells (PSCs).^{3,4} These organic-inorganic hybrid perovskite compounds adopt the ABX₃ perovskite structure, which involves a network of corner-sharing of [BX₆]⁴⁻ octahedra, where the B atom is a divalent metal cation (typically Pb^{II} or Sn^{II}) and X is a monovalent anion (typically Cl⁻, Br⁻ or I⁻), with the A monovalent cations (CH₃NH₃⁺ or HC(NH₂)₂⁺) occupying 12-fold coordinated holes within the structure and counterbalancing the charge of the [BX₆]⁴⁻. The outstanding photovoltaic performance of such perovskites are due to excellent optical and electronic properties, including high absorption coefficient,⁵ direct and tunable band gap,⁶ low charge recombination rates, structural phase dependence,⁷ and high charge carrier mobility.⁸ The power conversion efficiency of PSCs has increased rapidly, achieving more than 25% in less than a decade,⁹ which is much higher than those achieved by other

emerging thin film solar cell.¹⁰ In addition to having high efficiency, PSCs can be prepared with low cost materials and techniques, making them extremely interesting for large scale commercialization.

Many growth methods, such as spin and dip coating,¹¹⁻¹³ thermal evaporation,¹⁴ and solid-state reaction,^{15,16} have been developed to prepare MAPbI₃ perovskites with different morphologies. Besides the formation of thin films of MAPbI₃ for solar cells, other regular morphologies, such as microwires,¹⁷⁻¹⁹ nanowires²⁰ and quantum dots,²¹ have been produced. The identification of their crystal growth mechanism is crucial for understanding their fundamental chemical and physical properties. The solvothermal method is an efficient route to synthesize MAPbI₃ materials due to its advantages of relatively low temperatures, single-step process, and high reproducibility.^{22,23} High quality and uniform cuboid shaped MAPbI₃ perovskite crystals have been synthesized via solvothermal method using an autoclave.^{24,25} Recent studies^{26,27} have shown that the reaction temperature is one of the keys to being able to predictably control the crystal and film growth. In this work, MAPbI₃ was synthesized by a solution method through systematically controlling precursor concentration and reaction temperature. We observed an interesting evolution of morphology during the perovskite growth, from irregular particles to well-defined cubic morphology. Also, MAPbI₃ hopper cubes appear due to extreme supersaturation condition in the reaction medium, caused by relatively

*e-mail: joseantonio.souza@ufabc.edu.br

Editor handled this article: Pedro H. C. Camargo (Associate)

high concentration of PbI₂ and low temperature. The mechanisms of crystal growth and morphology evolution were discussed in detail.

Experimental

Sample preparation

Crystals of MAPbI₃ perovskite were obtained by a solution method similar to the one previously reported.²⁸ All chemical reagents were directly used without further purification. In a typical experimental process, 50–200 mg (0.1–0.4 mmol) of lead iodide (PbI₂, Sigma-Aldrich, St. Louis, USA) was completely dissolved in 1 mL of hydriodic acid (HI, 45 wt. % in water, Sigma-Aldrich, St. Louis, USA), then 30 mL of isopropyl alcohol (IPA, Synth, Diadema, Brazil) were added under stirring. The solution was subjected to different reaction temperatures ($T = -50, 0, 30, 55$ and 80 °C), then 0.3 mL of methylamine (CH₃NH₂, 40% in water, Sigma-Aldrich, St. Louis, USA) was added dropwise, and the final solution was stirred for 1 min. The black precipitates were collected by centrifugation in room temperature. The samples were washed with IPA until the supernatant was colorless and then dried at desiccator overnight.

Sample characterization

For the identification of the crystalline phases of the samples, X-ray diffraction (XRD) measurements were performed. These measurements were obtained using a diffractometer STADI-P model of Stoe (Darmstadt, Germany) with Mo K α_1 radiation whose wavelength is $\lambda = 0.7093$ Å. In a first analysis, the space group symmetry was confirmed using the Search-Match database. The study of morphological properties of the samples was carried out by using the scanning electron microscopy (SEM) JSM-670LA (Jeol, Tokyo, Japan). UV-Vis absorption spectra were collected using an ultraviolet-visible (UV-Vis) spectrometer (Shimadzu, Kyoto, Japan) and emission spectra were measured using a fluorescence steady state spectrometer (PicoQuant FluoTime 300, Berlin, Germany).

Results and Discussion

The concentration of lead precursor and the reaction temperature have great impact on the growth of perovskite crystals in the solution method as presented here. The MAPbI₃ crystals precipitates in IPA with adding of precursors reagents and HI, then the chemical reaction to form MAPbI₃ can be reached. The volatile methylamine

aqueous solution is added in excess, which will push the reaction to the formation of MAPbI₃ due to a shift of equilibrium, leading to crystallization of perovskite. Previous works^{28–30} reported that the MAPbI₃ crystals presents a tetragonal phase at room temperature with a thermodynamic favored morphology of cubes. In order to investigate and understand the crystal growth process and shape-evolution of the MAPbI₃ particles, we have performed a series of experiments using different reaction temperature and different concentrations of PbI₂, leading to an interesting observation on the cubic morphology of the perovskite particles. First, we performed experiments at low temperatures ($T = 0$ and -50 °C) with 0.1 mmol PbI₂. As shown in Figures 1a and 1b, the samples obtained at $T = -50$ °C presented an irregular round-shaped particles of average size of 0.9 ± 0.2 μm , while at $T = 0$ °C the irregular particles have been evolved into cubic shape morphology with smooth edges and particle size of 1.1 ± 0.2 μm . In contrast with the small irregular particles obtained at low temperature, the perovskite particles obtained at high temperatures reveal well-defined cubic shape of MAPbI₃ perovskite. The samples prepared at $T = 80$ °C reveal microcubes of MAPbI₃ perovskite with average particle size of 9 ± 3 μm . As can be seen in Figure 1, an interesting morphology evolution process from irregular to cubic particles is observed by increasing the reaction temperature from $T = -50$ to $T = 80$ °C. The increase of the average size of the perovskite particles as a function of temperature is also presented in the Figure 1d. We have also analyzed the optical properties of the MAPbI₃ samples. In our analysis, the band gap energy of the perovskite samples does not change, regardless of the synthesis condition. The absorption spectrum of perovskite microcubes prepared at $T = 80$ °C shows an abrupt decrease of absorption around 800 nm. The band-to-band optical transition was determined by the Tauc plot, presented in the inset of Figure 2a, from the UV-Vis absorption spectra for a direct bandgap semiconductor without excitonic effects. The zero-crossing point gives a band gap energy (E_g) of 1.47(1) eV for MAPbI₃ samples which agrees with literature.³¹ Figure 2b shows the photoluminescence (PL) spectra of MAPbI₃ samples. The PL peak of MAPbI₃ is assigned to 793 nm for all samples, leading to an experimental value of $E_g = 1.56$ eV.

Although the MAPbI₃ morphology is synthesis parameter dependent, the crystal structure remains tetragonal with the same space group symmetry for all samples. Figure 3 shows structural characterization of MAPbI₃ synthesized at $T = 80$ °C, using 0.1 mmol of PbI₂. X-ray diffraction (XRD) pattern indicates the expected Bragg reflection positions considering *I4/mcm* space group symmetry (COD ID 4124388) in agreement with

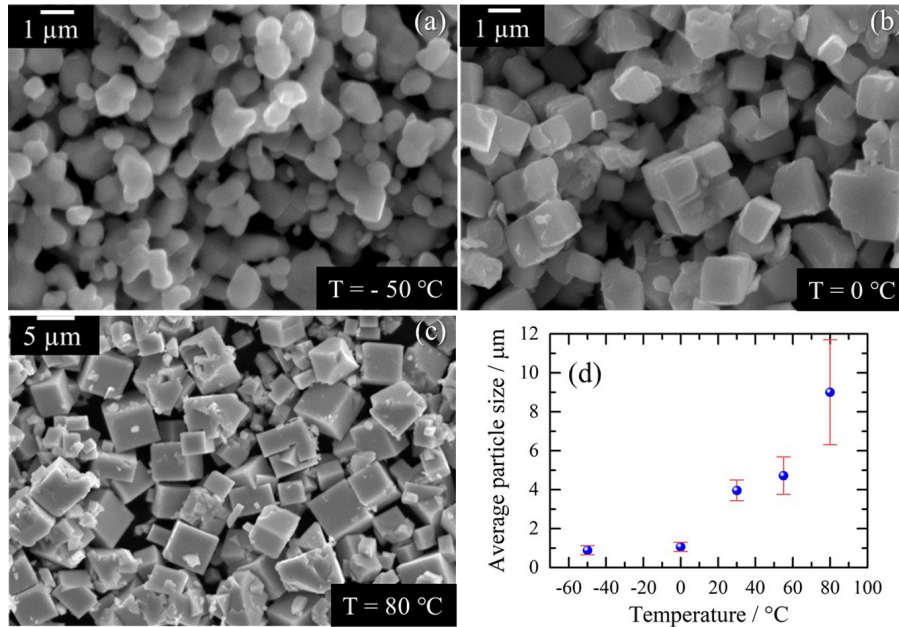


Figure 1. SEM images of MAPbI₃ prepared at (a) T = -50 °C, (b) T = 0 °C and (c) T = 80 °C. (d) Average particle size as a function of reaction temperature.

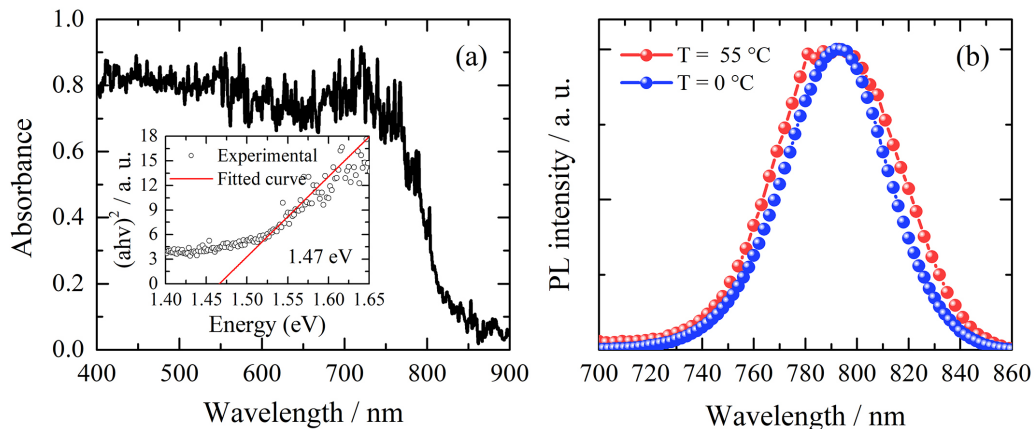


Figure 2. (a) UV-Vis spectrum of hybrid MAPbI₃ perovskite synthesized at T = 80 °C. Inset: Tauc plot fitting from the UV-Vis absorption spectra. (b) Normalized photoluminescence spectra of MAPbI₃ samples synthesized at T = 0 and 55 °C.

literature.³² Some traces of PbI₂ are observed at 2θ = 11.8 and 18°. Rietveld refinement shows a PbI₂ volume fractions of 0.6%. Different from other systems, this small fraction of impurity phase is negligible.³³ Lattice parameters refined for tetragonal perovskite are a = b = 8.850 Å and c = 12.637 Å. The MAPbI₃ has a three-dimensional (3D) structure where the methylammonium MA is at the center of the crystal while [PbI₆]⁴⁻ octahedral is in each corner of the tetragonal structure. The ammonium group on each MA hydrogen bonds to iodine in the perovskite structure. Interestingly, although the particle size decreases, there are no significant change on the XRD pattern when varying the reaction temperature using the same PbI₂ concentration. We have analyzed and compared the full width at half maximum (FWHM) of (002), (110), (004) and (220) Bragg reflections of each XRD pattern (Figure 4). Interestingly, the FWHM

reveals no significant change in the crystallite size regardless the change in reaction temperature (57 ± 4 nm).

In the sequence, a systematic study varying both temperature reaction and PbI₂ concentration was performed. Two main results can be observed in the sequence of the experiments through SEM investigations summarized in Figure 5. First, as we have already showed in the results presented above, the cubic-shaped particles increase in length with increasing of the reaction temperature. In the MAPbI₃ synthesis, all the precursors are present as ionic species in an alcohol solution. First, the PbI₂ is dissolved in the presence of HI in an alcohol solution. Then, the black crystals of perovskite begin to precipitate almost instantly after the addition of MA aqueous solution at room temperature. Among the precipitated perovskite microcubes, it was also observed cuboid aggregates (see

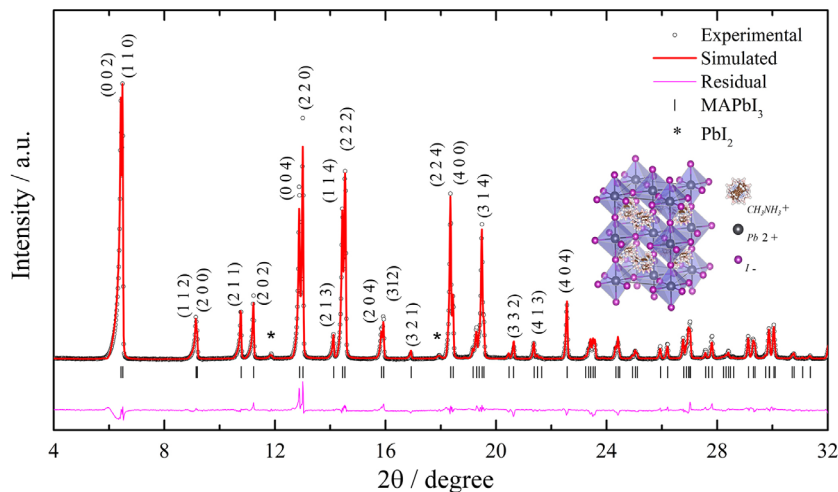


Figure 3. X-ray powder diffraction of perovskite MAPbI₃ samples obtained at T = 80 °C with 0.1 mmol of PbI₂.

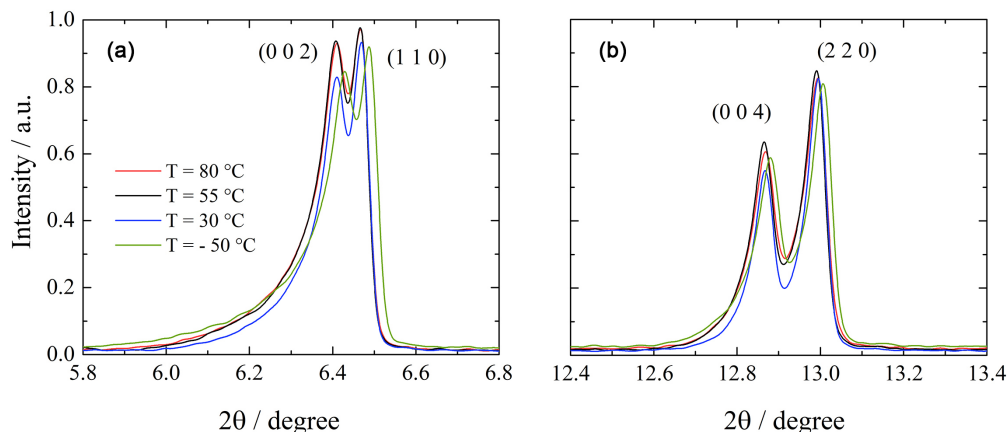


Figure 4. Selected reflections of the samples synthesized with 0.1 mmol of PbI₂. (a) (002) and (110) reflections and (b) (004) and (220) reflections of different reaction temperatures of MAPbI₃ synthesis.

Figure S1, Supplementary Information (SI) section), consisting of smaller particles (0.8–2 μm). Therefore, the growth of larger microcubes may be explained by the well-known Ostwald ripening mechanism. This ripening process is a thermodynamically driven spontaneous process, where the larger particles are more energetically favored.³⁴ In this process of subsequent growth, the dissolved species from small crystals are redeposit on the surface of larger crystals, increasing the particle size. Therefore, the Ostwald ripening is another growth mechanism that may be considered for the process of growth in the perovskite crystals.

In addition to the growth of perovskite particles with temperature, another growth mechanism is observed for samples prepared with higher concentration of PbI₂ (0.4 mmol of PbI₂). For these samples prepared at T = 30, 55 and 80 °C (Figure 5), it can be observed the presence of microcubes with hollow spaces, i.e., the interior spaces of the microcubes are not completely filled (Figure 6). The formation of these hollow spaces is usually called hopper morphology and occurs at relatively high supersaturations.³⁵

The cubic hopper morphology growth occurs at antisolvent crystallizations, where the supersaturation is higher near the edges and corners of the cubes than at the center of the six flat faces on growing crystals. This effect is called Berg effect and it favors two-dimensional (2D) nucleation, forming steps and depressions at the flat faces.³⁴ Under this condition of supersaturation, the nucleation and the crystal growth rates are very high causing the precursors to be quickly consumed.³⁶ Therefore, the hopper growth is a result of a kinetic effect. It is known that the transition between the cubic and such hopper growth happens at a determined supersaturation where the growth rate of the cubic crystal reaches a maximum.³⁵ Here, the perovskite crystals transferred from cubic to hopper-faced cuboid morphology when using high concentrations of PbI₂. Therefore, the excess of Pb and I ions limit the cubic growth by incorporating ions into the surface and the only way to incorporate more ions from the supersaturated solution is creating new surfaces. The edges of the first cubic core serve as a point for the 2D nucleation of a new cubic crystal.

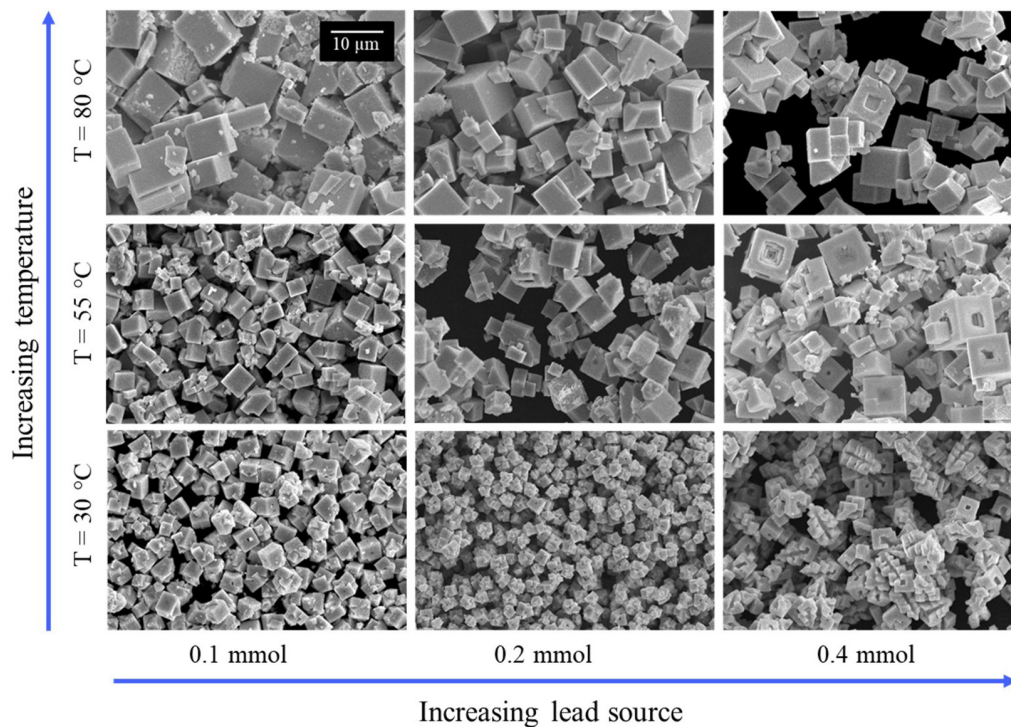


Figure 5. Morphology evolution process of MAPbI₃ particles by changing reaction temperature and PbI₂ concentration.

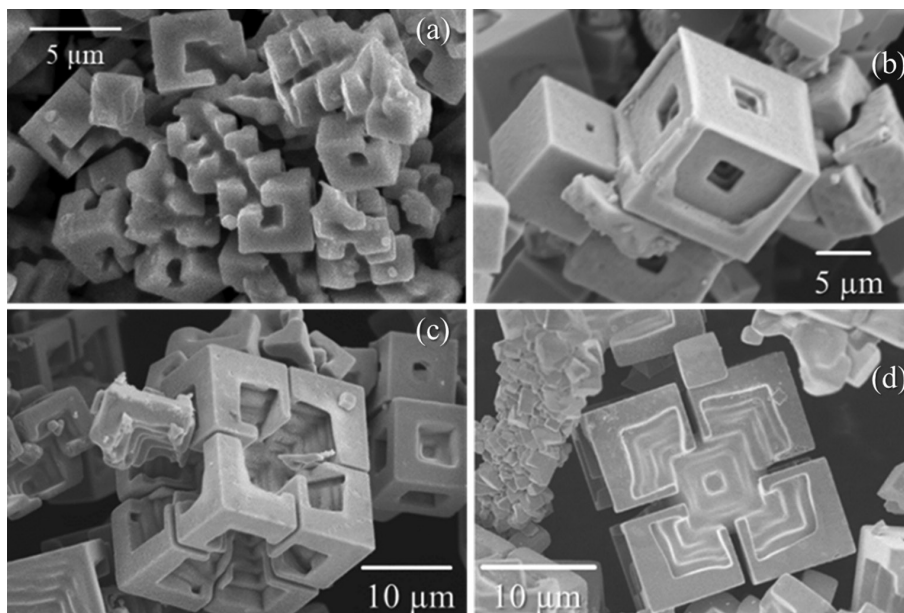


Figure 6. SEM images of hopper crystals of MAPbI₃ at (a) T = 30 °C, (b) T = 55 °C, (c) and (d) T = 80 °C. The PbI₂ concentration of all the samples is 0.4 mmol.

At room temperature ($T = 30\text{ }^{\circ}\text{C}$), where the supersaturation at the onset of precipitation should be higher, the dynamics of hopper growth appear as an assembly of interconnected cubic crystals and branches of hopper morphology, resulting from rapid consumption of supersaturation in a very short time. At intermediate temperature ($T = 55\text{ }^{\circ}\text{C}$), the particles grow bigger, and hopper cubes are still formed. When the reaction is high

($T = 80\text{ }^{\circ}\text{C}$), the thermodynamic growth (cubic growth) is favored rather than hopper growth, although the presence of hopper cubes is still present (hopper cubes are minority in the samples prepared at higher temperatures). Analyzing the XRD patterns of the different samples produced with different concentration of PbI₂, we can observe that when the supersaturation is higher, more {001} facets are exposed during the crystal growth. It is known that the depressions

caused by the hopper growth usually occur at the centers of the {001} facets of the cubic crystals.^{34,37,38} According to our XRD analysis, the most intense peak is referred to (110) plane at $T = 80\text{ }^{\circ}\text{C}$, followed by (002). When the PbI₂ concentration is increased, the relative intensity of the (002) diffraction peak also increases (see Figure S2, SI section). Furthermore, the intensity of the (002) peak is higher for lower reaction temperatures, coinciding with the scenario where the hopper morphology is predominant. Then, the {001} facets are mostly exposed when the hopper growth takes place on the perovskite crystal growth process.

At equilibrium conditions, crystal shape is driven to achieve the minimum total surface free energy. Crystals grow faster in the direction perpendicular to the face with the higher surface energy, resulting in elimination or reduction of higher energy surfaces, while lower energy surfaces increase in area.^{39,40} The average surface energies of different facets follow the order for the perovskite structure: $\{111\} > \{110\} > \{100\}$.⁴¹ For the MAPbI₃ tetragonal perovskites, the predicted morphology is a cube/polyhedron formed by the slow growth of (002) and (110) planes (lower energy surfaces; see Figure S3, SI section). However, the thermodynamics and kinetics of the crystal growth can be affected by impurities, ions, molecules that constitute the growth medium, precursors concentration and reaction temperature, thus altering the morphology. A theoretical analysis on the crystallization of MAPbI₃ and the control of grain sizes in the two-step thin films formation were previously reported.⁴² Deriving a thermodynamic reaction model equation from Gibbs free energy, they demonstrate that the reaction temperature is a critical factor affecting grain size. Accordingly, at low temperature, we expect that the number of nuclei increases and, therefore, the size of the particles decreases. Following the thermodynamic model, we would expect a faster nucleation at low temperatures, resulting in a slow particle size growth. Indeed, we have observed smaller particles when decreasing the reaction temperature. At low temperature ($T = -50\text{ }^{\circ}\text{C}$), the crystals grow at nonequilibrium conditions, and the growth of crystals is no more thermodynamically driven. Therefore, the various planes grow at the same rates, yielding small particles with irregular spherical morphology. As the temperature increases to $T = 0\text{ }^{\circ}\text{C}$, the facets {001} and {110} starts to increase in area, forming the cubic-like morphology with smooth edges. However, the size of these cubes is smaller than those obtained at higher temperatures. When the reaction temperature reaches $T = 80\text{ }^{\circ}\text{C}$, the reaction conditions turn into a thermodynamic controlled scenario (near the equilibrium condition). In this scenario, cubes with {001} and {110} facets prefer to grow.

Many theories focused mainly on the crystal growth in

near equilibrium conditions, but the crystal growth theories in nonequilibrium conditions are still limited. For example, the Wulff construction predicts the shape of an equilibrium crystal, according to the Gibbs thermodynamic principle, by minimizing the total surface free energy associated to the crystal-medium interface.^{43,44} Also, the Bravais, Friedel, Donnay and Harker (BFDH) method used to predict the morphology of MAPbI₃ in this work (see Figure S3, SI section) do not consider the environmental growth medium.⁴⁵ Therefore, in nonequilibrium conditions (as supersaturated growth environments presented here), environmental growth medium and crystal growth kinetics should be considered. Recently, the supersaturation-controlled surface structure strategy, which is derived from thermodynamics and the Thomson-Gibbs equation, has been proposed.⁴⁶ According to this study, the exposed crystal faces can be simply tuned by controlling the supersaturation. In summary, when the supersaturation is low (near the equilibrium condition), crystal facets with low surface energy prefer to be exposed, which is in accordance with the shapes predicted by the thermodynamic models. On the other hand, when the supersaturation is extremely high, various crystal facets would have similar crystal growth rates, which results in the formation of spherical crystals.⁴⁷ In our first experiment, the reaction temperature is changed, but the concentration of PbI₂ is the same for all samples. In these conditions, we can consider that the supersaturation at the onset of precipitation is higher for the lowest reaction temperature ($T = -50\text{ }^{\circ}\text{C}$) since the solubility decreases with temperature. Accordingly, at high supersaturation conditions (low temperature), the crystal facets have similar crystal growth rates, leading to irregular rounded particles. On the other hand, at low supersaturation conditions (high temperature), crystal facets with low surface energy prefer to grow. In addition, another nonequilibrium condition is observed at high concentration of PbI₂ (high supersaturation). When the PbI₂ concentration is increased, the conditions are far from the equilibrium as well. In this scenario, the medium is highly supersaturated at onset of precipitation, leading to the growth of hopper crystals induced by kinetic effects. The hopper morphology is more pronounced at room temperature ($T = 30\text{ }^{\circ}\text{C}$), where the supersaturation is higher. Figure S7 (SI section) summarizes the growth and morphological evolution of the perovskites obtained under non-equilibrium and equilibrium conditions observed in this work.

Conclusions

We have shown an evolution in the perovskite particle morphology, which goes through irregular particles, and cubes with smoothed edges and corners, to well-

defined cubic morphology. The growth of well-defined cube morphology of MAPbI₃ perovskite is observed near equilibrium conditions, where the thermodynamic morphology is favored, i.e., at reaction temperatures of $T > 30$ °C. In the nonequilibrium conditions (low reaction temperatures and high concentration of PbI₂), the MAPbI₃ growth presents other morphologies. Growth process at very low temperature was mainly dominated by kinetic growth regimes, which results in irregular rounded particles. On the other hand, the hopper morphology, which characterizes the presence of steps or depressions in the center of the cube faces, appear when the supersaturation is relatively high. The growth evolution of these hybrid organic-inorganic perovskite particles was discussed and explained by considering thermodynamic and kinetic models.

Supplementary Information

Supplementary data (additional SEM images of perovskites microcubes; MAPbI₃ morphology predicted by BFDH method; particle size distribution of all MAPbI₃ samples; crystal structure report for MAPbI₃ tetragonal phase) are available free of charge at <http://jbcs.sbq.org.br> as PDF file.

Acknowledgments

This work is supported by the CAPES and the Brazilian agency CNPq under grant No. 305601/2019-9 and the FAPESP under grant Nos. 2018/14181-0, 2017/02317-2, and 2018/15682-3. The authors are grateful for the Multiuser Experimental Center of UFABC.

References

- Chen, Z.; Turedi, B.; Alsalloum, A. Y.; Yang, C.; Zheng, X.; Gereige, I.; AlSaggaf, A.; Mohammed, O. F.; Bakr, O. M.; *ACS Energy Lett.* **2019**, *4*, 1258.
- Yang, W. S.; Park, B.-W.; Jung, E. H.; Jeon, N. J.; Kim, Y. C.; Lee, D. U.; Shin, S. S.; Seo, J.; Kim, E. K.; Noh, J. H.; Seok, S. I.; *Science* **2017**, *356*, 1376.
- Azpiroz, J. M.; Mosconi, E.; Bisquert, J.; de Angelis, F.; *Energy Environ. Sci.* **2015**, *8*, 2118.
- Kumar, N.; Rani, J.; Kurchania, R.; *Mater. Today: Proc.* **2021**, *46*, 5570.
- Baikie, T.; Fang, Y.; Kadro, J. M.; Schreyer, M.; Wei, F.; Mhaisalkar, S. G.; Graetzel, M.; White, T. J.; *J. Mater. Chem. A* **2013**, *1*, 5628.
- Noh, J. H.; Im, S. H.; Heo, J. H.; Mandal, T. N.; Seok, S. I.; *Nano Lett.* **2013**, *13*, 1764.
- Bonadio, A.; Escanhoela Jr., C. A.; Sabino, F. P.; Sombrio, S.; de Paula, V. G.; Ferreira, F. F.; Janotti, A.; Dalpian, G. M.; Souza, J. A.; *J. Mater. Chem. A* **2021**, *9*, 1089.
- Wehrenfennig, C.; Eperon, G. E.; Johnston, M. B.; Snaith, H. J.; Herz, L. M.; *Adv. Mater.* **2014**, *26*, 1584.
- National Renewable Energy Laboratory (NREL); *Best Research-Cell Efficiencies*, <https://www.nrel.gov/pv/cell-efficiency.html>, accessed in March 2022.
- Yang, W. S.; Noh, J. H.; Jeon, N. J.; Kim, Y. C.; Ryu, S.; Seo, J.; Seok, S. I.; *Science* **2015**, *348*, 1234.
- Shen, H.; Duong, T.; Peng, J.; Jacobs, D.; Wu, N.; Gong, J.; Wu, Y.; Karuturi, S. K.; Fu, X.; Weber, K.; Xiao, X.; White, T. P.; Catchpole, K.; *Energy Environ. Sci.* **2018**, *11*, 394.
- Im, J. H.; Kim, H. S.; Park, N. G.; *APL Mater.* **2014**, *2*, 081510.
- Burschka, J.; Pellet, N.; Moon, S. J.; Baker, R. H.; Gao, P.; Nazeeruddin, M. K.; Grätzel, M.; *Nature* **2013**, *499*, 316.
- Liu, M.; Johnston, M. B.; Snaith, H. J.; *Nature* **2013**, *501*, 395.
- Prochowicz, D.; Franckevičius, M.; Cieślak, A. M.; Zakeeruddin, S. M.; Grätzel, M.; Lewiński, J.; *J. Mater. Chem. A* **2015**, *3*, 20772.
- Chen, L.; Tang, F.; Wang, Y.; Gao, S.; Cao, W.; Cai, J.; Chen, L.; *Nano Res.* **2015**, *8*, 263.
- Zhu, C.; Tang, Y.; Chen, F.; Manohari, A. G.; Zhu, Y.; Shi, Z.; Xu, C.; *J. Cryst. Growth* **2016**, *454*, 121.
- Bonadio, A.; de Oliveira, L. S.; Polo, A. S.; Souza, J. A.; *CrystEngComm* **2019**, *21*, 7365.
- Bonadio, A.; Sabino, F. P.; Tofanello, A. M.; Freitas, A. L.; de Paula, V. G.; Dalpian, G. M.; Souza, J. A.; *J. Phys. Chem. C* **2021**, *125*, 15636.
- Zhu, H.; Fu, Y.; Fei, M.; Wu, X.; Gong, Z.; Ding, Q.; Gustafsson, M. V.; Trinh, M. T.; Jin, S.; Zhu, X. Y.; *Nat. Mater.* **2015**, *14*, 636.
- Zhu, Z. Y.; Yang, Q. Q.; Gao, L.-F.; Zhang, L.; Shi, A.-Y.; Sun, C.-L.; Wang, Q.; Zhang, H.-L.; *J. Phys. Chem. Lett.* **2017**, *8*, 1610.
- Zhang, B.; Guo, F.; Xue, J.; Yang, L.; Zhao, Y.; Ge, M.; Cai, Q.; Liu, B.; Xie, Z.; Chen, D.; Lu, H.; *Sci. Rep.* **2017**, *7*, 17695.
- Zhang, T.; Yang, M.; Benson, E. E.; Li, Z.; van de Lagemaat, J.; Luther, J. M.; Yan, Y.; Zhu, K.; Zhao, Y.; *Chem. Commun.* **2015**, *51*, 7820.
- Chen, Y.; Yang, S.; Xiao, C.; Zheng, Y. C.; Hou, Y.; Li, Y. H.; Zeng, H. D.; Yang, H. G.; *J. Mater. Chem. A* **2015**, *3*, 15854.
- Zhang, B.; Guo, F.; Yang, L.; Jia, X.; Liu, B.; Xie, Z.; Chen, D.; Lu, H.; Zhang, R.; Zheng, Y.; *J. Cryst. Growth* **2017**, *459*, 167.
- Raghav, A.; Singh, S.; Sharma, S. K.; Kabra, D.; Bag, M.; Satapathi, S.; *Nano-Struct. Nano-Objects* **2017**, *12*, 106.
- Ren, Y. K.; Ding, X. H.; Wu, Y. H.; Zhu, J.; Hayat, T.; Alsaedi, A.; Xu, Y. F.; Li, Z. Q.; Yang, S. F.; Dai, S. Y.; *J. Mater. Chem. A* **2017**, *5*, 20327.
- Guo, F.; Zhang, B.; Wang, J.; Ba, H.; Guo, R.; Huang, Y.; Ren, P.; *Opt. Mater. Express* **2017**, *7*, 4156.

29. Yang, S.; Zheng, Y. C.; Hou, Y.; Chen, X.; Chen, Y.; Wang, Y.; Zhao, H.; Yang, H. G.; *Chem. Mater.* **2014**, *26*, 6705.
30. Chen, Y.; He, M.; Peng, J.; Sun, Y.; Liang, Z.; *Adv. Sci.* **2016**, *3*, 1500392.
31. Matsuishi, K.; Ishihara, T.; Onari, S.; Chang, Y. H.; Park, C. H.; *Phys. Status Solidi B* **2004**, *241*, 3328.
32. Yamada, Y.; Yamada, T.; Phuong, L. Q.; Maruyama, N.; Nishimura, H.; Wakamiya, A.; Murata, Y.; Kanemitsu, Y.; *J. Am. Chem. Soc.* **2015**, *137*, 10456.
33. Ramirez, F. E. N.; Pasca, G. A. C.; Souza, J. A.; *Phys. Lett. A* **2015**, *379*, 1549.
34. Liu, B.; Hu, X. In *Advanced Nanomaterials for Pollutant Sensing and Environmental Catalysis*, 1st ed.; Zhao, Q., ed.; Elsevier: Amsterdam, The Netherlands, 2020, ch. 1.
35. Sunagawa, I.; *Forma* **1999**, *14*, 147.
36. Desarnaud, J.; Derluyn, H.; Carmeliet, J.; Bonn, D.; Shahidzadeh, N.; *J. Phys. Chem. Lett.* **2018**, *9*, 2961.
37. Zhu, J. P.; Yu, S. H.; He, Z. B.; Jiang, J.; Chen, K.; Zhou, X. Y.; *Chem. Commun.* **2005**, *46*, 5802.
38. Zhu, T.-J.; Chen, X.; Cao, Y.-Q.; Zhao, X.-B.; *J. Phys. Chem. C* **2009**, *113*, 8085.
39. Choi, K.-S.; *Dalton Trans.* **2008**, *40*, 5432.
40. Hwang, N. M.; *Non-Classical Crystallization of Thin Films and Nanostructures in CVD and PVD Processes*, 1st ed.; Springer: Dordrecht, The Netherlands, 2016.
41. Huang, K.; Yuan, L.; Feng, S.; *Inorg. Chem. Front.* **2015**, *2*, 965.
42. Ahn, N.; Kang, S. M.; Lee, J. W.; Choi, M.; Park, N. G.; *J. Mater. Chem. A* **2015**, *3*, 19901.
43. Wulff, G.; *Cryst. Mater.* **1901**, *34*, 449.
44. Peev, N. S.; *Cryst. Res. Technol.* **2017**, *52*, 1700100.
45. Winn, D.; Doherty, M. F.; *AIChE J.* **2000**, *46*, 1348.
46. Lin, H. X.; Lei, Z. C.; Jiang, Z. Y.; Hou, C. P.; Liu, D. Y.; Xu, M. M.; Tian, Z. Q.; Xie, Z. X.; *J. Am. Chem. Soc.* **2013**, *135*, 9311.
47. Chen, W.; Kuang, Q.; Xie, Z.; *Sci. China Mater.* **2015**, *58*, 281.

Submitted: September 27, 2021

Published online: March 30, 2022

